Measuring the Length Distribution of a Fibril System: A Flow Birefringence Technique Applied to Amyloid Fibrils

Salman S. Rogers,*,† Paul Venema,‡ Leonard M. C. Sagis,‡ Erik van der Linden,‡ and Athene M. Donald†

Department of Physics, Cambridge University, Cavendish Laboratory, Cambridge CB3 0HE, UK, and Laboratory of Food Physics, Wageningen University, P.O. Box 8129, 6700 EV Wageningen, The Netherlands

Received December 15, 2004; Revised Manuscript Received January 25, 2005

ABSTRACT: Relaxation of flow birefringence can give a direct measure of the rotational diffusion of rodlike objects in solution. With a suitable model of the rotational diffusivity, a length distribution can be sought by fitting the decay curve. We have measured the flow birefringence decay from solutions of amyloid fibrils composed of β-lactoglobulin and extracted a length distribution using the Doi−Edwards−Marrucci−Grizzuti theory of semidilute rotational diffusion. The concentration scaling of the results shows that the fibrils diffuse as free rods: they cannot be significantly branched, sticky, or break up under dilution. The length distribution obtained shows a single broad peak, consistent with measurements of the fibrils by electron microscopy. This comparison, and combination of the experiment with an assay to find the total concentration of fibrils, allows calibration of the length scale and concentration scale of the length distribution. It is our hope that this method can be used for following the growth kinetics of amyloid fibrils in vitro and for studying the length distribution of rodlike systems in general.

1. Introduction

A wide range of proteins are known to misfold and aggregate in mildly denaturing conditions into rodlike structures known as amyloid fibrils. The proteins are thought to be held together by continuous intermolecular β-sheets which run along the fibril axis.[1,2] This common structural motif, dependent only on the peptide backbone, as well as the observation that a wide variety of proteins form these fibrils, suggests that amyloid fibrils are a generic form of protein structure, largely independent of primary structure.[3] For this reason, the self-assembly of proteins into amyloid fibrils is inherently interesting as a simple example of protein interaction and folding, quite apart from their link to a number of degenerative diseases such as Alzheimer's and Parkinson's diseases.[4−7]

The kinetics of formation of amyloid fibrils has been studied for several protein systems but is not well understood. There is a nucleation event, involving misfolded proteins, oligomeric intermediates, surfaces, or "seeds", followed by a growth period, in which proteins join onto one or both ends of the new fibril (see e.g. ref 8). Various mechanisms have been proposed for the nucleation and growth kinetics, but these remain largely qualitative and speculative. One of the difficulties in following the kinetics of fibril formation is the lack of accurate assays for measuring fibril concentration or growth rate and the absence of information on the fibril length distribution.

β-Lactoglobulin (β-lg) solutions form amyloid fibrils under prolonged heating at low pH and low ionic strength.[9,10] These fibrils are polydisperse in length $\sim$1 μm and monodisperse in cross section, with a width of about 4 nm.[9,11] The persistence length, as obtained from transmission electron microscopy, is approximately 1.6 μm—of the same order of magnitude as the length.[12] At conditions of pH 2, 5 mg/mL concentration, 0.01 M ionic strength, and heating at 80 °C, transparent solutions of fibrils are produced without macroscopic aggregates.[12,13] The fibrils show a twisted strand structure, one or two protein monomers across in cross section.[11,13] The transparency of β-lg (and other amyloid) fibril solutions is to be expected since the volume of a fibril is much less than the cube of the wavelength of visible light. Hence, light scattering and form birefringence/dichroism are low.

Measuring the length distribution of this system has proven difficult. It seems that the only widely applicable method of measuring a length distribution of rodlike or fibrillar solutions and suspensions has been by direct imaging; for amyloid fibrils this is possible with transmission electron microscopy (TEM). Yet it is hard to get length distributions with this technique primarily because of the difficulty of measuring enough lengths to get good statistics. Problems such as variations in contrast, the semiflexibility, and overlapping nature of the fibrils and irregularities in the supporting Formvar film conspire to make automated image analysis impractical. The simple problem of imaging enough fibrils at a magnification at which their widths are resolved forces us to make composite images. This alone can be difficult, especially when the Formvar film is gradually tearing and deforming because of damage by the electron beam. Besides these technical difficulties, unanswered physical questions include whether fibrils are likely to fracture or disaggregate in TEM sample preparation and whether longer or shorter fibrils may be more likely to be adsorped onto the TEM grid's surface. Often fibrils are seen which appear to have splintered *after* being adsorbed (see Figure 1).

Despite the difficulties, techniques of measuring length distributions of fibrils are important in the study of several different kinds of materials apart from

* To whom correspondence should be addressed. E-mail ssr24@phy.cam.ac.uk.
† Cambridge University.
‡ Wageningen University.

10.1021/ma0474224 CCC: $30.25
Published on Web 03/03/2005

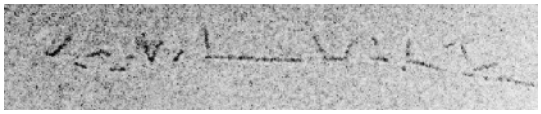

Figure 1. A splintered β-lg fibril, imaged by TEM.

amyloid fibrils, such as cellulose fibrils,[14,15] nanotubes,[16,17] nanowires,[18] and rodlike mineral particles such as clays,[19,20] asbestos fibrils,[21−23] etc.

A range of methods are known for obtaining size or length distributions via relaxation measurements, and these have been developed to varying extents. They share a central feature: that the relaxation of a system is based on the diffusion of its constituents. Therefore, in principle, parameters which affect diffusion rate, such as size or concentration of particles, can be extracted. Some of these methods are well-known, such as dynamic light scattering and diffusing wave spectroscopy,[24] for weakly scattering and turbid systems, respectively. For birefringent or dichroic systems, rheooptics[25,26] and electrooptics[27,28] have been used to extract diffusion information and material parameters. However, as far as we are aware, ours is the first published technique of relaxation measurements and accompanying data analysis which both produce a detailed length distribution and can be applied to a polydisperse system of filaments such as amyloid fibrils.

2. Theoretical Section

2.1. Approaching the Length Distribution from Rheooptical Measurements. Rheooptics is the study of the relationships between flow conditions and optical properties in a material. It is a useful probe of complex fluids because the optical properties often depend directly on the microscopic structure if the fluid is transparent.[29] In the case of a suspension of rodlike objects with anisotropic electric polarizability or absorptivity, measurable birefringence or linear dichroism may result if there is an overall alignment of the particles caused, for example, by shear flow. In general, this can be formalized by considering a complex refractive index tensor, n_{ij}. For clear and optically thin samples, n_{ij} simply depends on the sum of the contributions of all the particles in suspension. We treat amyloid fibrils as stiff, nonsticky rods, an assumption which will be examined in section 2.3. As we have already argued, scattering and form birefringence/dichroism are low and can be ignored. Thus, only the intrinsic polarizability of the fibrils contributes to the birefringence, and the refractive index takes the form[30]

$$n_{ij} = \sum_{\text{all rods in unit volume}} \frac{4\pi}{18}\frac{(\bar{n}^2+2)^2}{\bar{n}}[\alpha_2\delta_{ij} + (\alpha_1-\alpha_2)u_iu_j] \quad (1)$$

where $\bar{n}$ is the isotropic refractive index of the system, α_1 and α_2 are the polarizabilities parallel and perpendicular to the rod axis, respectively, and $\mathbf{u}$ is the unit vector of orientation. It can be seen that the anisotropy in the refractive index, n_{12}, is proportional to an average over the orientations of the rods; therefore, measuring the birefringence gives a quantitative measure of the average orientation, the decay of which can be used to track the rotational diffusion of the rods during a relaxation experiment.

2.2. Linking Rotational Diffusion to Rod Lengths. Intuitively, it is obvious that shorter rods will diffuse faster than longer ones. However, to extract quantitative information on the length of the rods, a suitable model of the diffusivity is required. The rotational diffusivity of noninteracting rods with diameter d and length L in a fluid of viscosity η is given by[31]

$$D_r^0 = \frac{k_BT\log(L/d)}{3\pi\eta L^3} \quad (2)$$

In a dilute solution, the rods diffuse unhindered by each other (this may be regarded as the definition of "dilute" in a rod solution.) Under shear, this coefficient may then be used to calculate the birefringence.

However, long, thin rods in a solution may overlap and hinder each others' diffusion even if the volume fraction is still very low. This is known as the semidilute regime and applies for concentration c in the range $1/L^3 \ll c \ll 1/L^2d$. Doi and Edwards[31] developed a model for this diffusion in which rods may move freely longitudinally but are constrained laterally within a tube defined by the positions of the nearest neighours. Rods may only rotate by a combination of longitudinal diffusion and rotational diffusion through small angles within the tube. This leads to a rotational diffusivity (for an isotropic orientational distribution) of

$$D_r^{\text{iso}} \approx \beta\left(\frac{a_c}{L}\right)^2 D_r^0 = \frac{\beta D_r^0}{(cL^3)^2} \quad (3)$$

where a_c is the tube radius and β is an undetermined constant. The diffusion now depends on concentration and has a much higher dependence on the length of the rods. However, if the rods are not oriented isotropically, because of shear flow or other causes, a_c will depend on the orientational distribution of the rods, $\psi(\mathbf{u})$. This may be expanded in terms of spherical harmonics with coefficients b_{lm} to give the diffusivity[31]

$$D_r = D_r^{\text{iso}}\left(1 - 8\pi\sum_{l=2;\text{even}}^{\infty}\sum_{m=0}^{l}\frac{l-1}{l+2}\left[\frac{(l-3)!!}{l!!}\right]^2 {b_{lm}}^2\right)^{-2} \quad (4)$$

where the double factorial is defined as $n!! = n(n-2)\cdot(n-4)...5\cdot3\cdot1$ for $n > 0$ odd, $n!! = n(n-2)(n-4)...6\cdot4\cdot2$ for $n > 0$ even, and $n!! = 1$ for $n = -1, 0$. The coordinate frame, spherical harmonics, and coefficients b_{lm} are defined in Appendix A.

Marrucci and Grizzuti[32,33] proposed an extension to this theory for polydisperse systems (the DEMG theory). The diffusivity of each length component L_i, with concentration c_i, is given by[34]

$$D_{ri} = \frac{\beta k_BT}{\eta}L_i^{-4}\Big(\sum_m c_mL_mQ_{im}\Big)^{-1}\Big\{\sum_{j\le i}c_jL_j^4Q_{ij} + L_i^3\sum_{j>i}c_jL_jQ_{ij}\Big\}^{-1} \quad (5)$$

where

$$Q_{ij} = 1 - 8\pi\sum_{l=2;\text{even}}^{\infty}\sum_{m=0}^{l}\frac{l-1}{l+2}\left[\frac{(l-3)!!}{l!!}\right]^2 b_{lm,i}b_{lm,j} \quad (6)$$

and where L_1, L_2, L_3, ... are enumerated in increasing order of length. The boundary of the semidilute regime

now depends on the rod length: shorter rods may be unentangled while longer ones obey the DEMG theory. Defining the entanglement length L^* as

$$L^* = \frac{1}{\sqrt{\sum_i c_i L_i}} \tag{7}$$

rods of length significantly greater than L^* are in the semidilute regime. In a flow with shear rate γ, the coefficients $b_{lm,i}$ are related by the equation of motion:[31]

$$\frac{db_{lm,i}}{dt} = -D_{ri} l\,(l+1) b_{lm,i} - \gamma \sum_{l'm'} (l, m|\Gamma|l', m') b_{l'm',i} \tag{8}$$

where $\gamma\Gamma$ is the operator yielding the differential change in $\psi(\mathbf{u})$ due to this shear flow of velocity $\gamma z\hat{x}$. Γ is defined in Appendix A.

The measurable quantities, i.e., the magnitude Δn and angle χ (relative to the direction of flow) of birefringence, for light propagating along the y axis, can be obtained from the theory by diagonalizing n_{ij} in the xz plane (eq 1):

$$\Delta n = M\sqrt{[\sum_i c_{L_i}\langle u_x{}^2 - u_z{}^2\rangle_i]^2 + 4[\sum_i cL_i\langle u_x u_z\rangle_i]^2} \tag{9}$$

$$\tan 2\chi = \frac{2\sum_i c_{L_i}\langle u_x u_z\rangle_i}{\sum_i c_{L_i}\langle u_x{}^2 - u_z{}^2\rangle_i} \tag{10}$$

where M depends on the anisotropy in polarizability ($\alpha_1 - \alpha_2$) per unit length and therefore is taken as a constant of the β-lg fibril system, $c_{L_i} \equiv c_i L_i$, the length concentration, and angular brackets denote an average over the entire ensemble of rods. The averages $\langle u_x{}^2 - u_z{}^2\rangle_i$ and $\langle u_x u_z\rangle_i$ are related to the spherical harmonics calculated in eq 8 via

$$\langle u_x{}^2 - u_z{}^2\rangle_i = \left(\frac{4\pi}{15}\right)^{1/2}(b_{22,i} - 3^{1/2} b_{20,i}) \tag{11}$$

$$\langle u_x u_z\rangle_i = -\left(\frac{4\pi}{15}\right)^{1/2} b_{21,i} \tag{12}$$

The Doi−Edwards theory has been tested by several groups who have verified the concentration and length scaling $D_r \sim c^{-2}L^{-9}$.[35,36] However, they have disagreed on the constant β which has been variously determined to be of the order 10^3−10^4,[35,37] even though Doi and Edwards expected it to be of order 1. One possible explanation is that rods do not need to diffuse so far to escape their tubes;[38] thus, it can be seen that a constant of $O(1)$ multiplying L could lead to a much larger prefactor in the diffusivity because of the high power dependence on L. In particular, it is likely that semiflexibility of the rods in solution leads to variability in this factor as discussed in ref 39. The DEMG theory has been tested on the flow birefringence of bidisperse collagen solutions[39] and quantitatively verified. This is encouraging for our purposes since collagen fibrils are very flexible: lengths are around 309 nm,[40] and the persistence length is much lower: 40−57 nm according to TEM estimates[41] and ∼170 nm as estimated from dynamic rheometric measurements.[42] β-lg fibrils are much stiffer as discussed below, so their motion is likely to be closer to that of rigid rods.

At higher concentrations than those of the semidilute regime, when $c \gg 1/L^2 d$, the longitudinal diffusion becomes constrained and liquid crystalline alignment or frustrated behavior arises. In this regime the relaxation of the orientational distribution becomes a cooperative process in which it would be much more difficult to extract quantitative information about the length distribution.

2.3. Can Fibrils Be Treated as Rods? Before applying the DEMG theory to amyloid fibrils, the assumption that fibrils diffuse like rods must be questioned.

There are many simple physical reasons why the fibrils might not: if they might stick to each other or are branched, we might expect a much higher dependence of diffusivity on concentration, since their motion would become much more constrained at increasing concentrations than the Doi−Edwards tube model envisages. Similarly, if they were too flexible, it is also likely that a theory of rods would not be able to describe them.

TEM studies have yielded some evidence to support the use of the DEMG theory. β-lg fibrils are observed to be unbranched (or at most rarely branched)[11,43] and are not found stuck together in flocs but randomly deposited on the TEM grids and easily washed off (refs 9 and 44, for example, and our own observations). The persistence length, obtained by measuring the end-to-end distance and contour length of fibrils by TEM, has been evaluated as 1.6 μm[12] and by static light scattering as >600 nm.[13] Moreover, the percolation concentration at which the β-lg fibril system becomes a solid or gel has also been found to be quantitatively consistent with a model of randomly packed, sterically/electrostatically repelling semiflexible rods (i.e., a rod glass), without the need to introduce cross-links, branches, or stickiness into the considerations.[45]

However, more conclusively than these results, the DEMG theory itself predicts a concentration dependence which we can use as a self-consistency test. If the fibril diffusion obeys the concentration scaling[39] of the theory when we successively dilute our samples, it is evidence that the fibrils do indeed diffuse according to the theory.

If we transform concentrations of each length component by a dilution factor ν, so that $c_i \rightarrow c_i/\nu$, the diffusivity in eq 5: $D_{ri} \rightarrow \nu^2 D_{ri}$. Thus, scaling the birefringence in steady shear or transient flow according to

$$\nu\Delta n = f(\gamma/\nu^2, \nu^2 t) \tag{13}$$

should put measured curves onto the same universal curve f. (Note that Δn also scales with ν according to eq 9.) If, however, the fibrils are short or dilute enough not to interact, we should expect no dependence of D_r on concentration. Thus, the birefringence will then scale according to

$$\nu\Delta n = f(\gamma, t) \tag{14}$$

which would also apply to any other relaxation process which does not depend on concentration.

In addition, verification of this scaling behavior tests the implicit assumption that the fibrils do not break up upon dilution. In fibril solutions prepared under our

chosen conditions described below, no aggregates except fibrils were easily found by TEM or light microscopy. Therefore, we feel justified in assuming that there is no significant effect except the flow alignment of fibrils that leads to the measured birefringence. (Scaling of experimental results is pursued in sections 4.1 and 4.2.)

2.4. The Inverse Problem: Fitting Birefringence Data with a Length Distribution. Equations 5−12 provide a complete prediction of flow birefringence given an arbitrary length distribution $\{c_i, L_i\}$ and shear history. We wish to do the opposite: find the length distribution by measuring flow birefringence. This is most easily done for the case of birefringence decay in stopped flow, since the problem is analogous to the inverse Laplace transform in the analysis of dynamic light scattering data. The decay $\Delta n(t)$ is a sum of decays from each length component c_i, L_i, but each decay is neither exponential nor independent of other components in the set $\{c_i, L_i\}$.

If the shear rate is high enough, we can make the approximation that the decay starts from total alignment at $t = 0$: i.e. $\psi(\theta, \phi) = \delta(\theta - \pi/2)\delta(\phi)$. However, since we are only using eq 8 for $t > 0$ when $\gamma = 0$, we may consider alignment at $\theta = 0$ instead and use the much simpler coefficients for $\psi(\theta, \phi) = \delta(\theta)$:

$$b_{lm,i} = \begin{cases} \sqrt{\dfrac{2l+1}{4\pi}} & \text{for } m = 0 \\ 0 & \text{otherwise} \end{cases} \tag{15}$$

From this, only the coefficients $b_{l0,i}$ are nonzero and need to be calculated for $t > 0$. Thus, computation can be made more efficient, and we have the additional advantage that eq 9 reduces to

$$M\sum_j K_{ij} c_{L_j} = \Delta n_i \tag{16}$$

where

$$K_{ij} = \langle u_x^{\,2} - u_z^{\,2} \rangle_j|_{t_i} \tag{17}$$

We can use this equation to solve for $\{c_{L_i}\}$ iteratively using a method based on that of Chapter 18.5 in ref 46. After choosing a suitable array of lengths $\{L_i\}$ and a corresponding initial estimate of $\{c_{L_i}\}$, we wish to adjust $\{c_{L_i}\}$ until it predicts the measured decay Δn_i at all points in time t_i. (Note that the length concentration c_{L_i} is proportional to the number of protein molecules in fibrils of length L_i, and thus, from the amyloid fibril point of view, it is a more relevant measure of concentration than the number of fibrils c_i.)

The "kernel" matrix K_{ij} is useful because it can be used to make iterative adjustments to c_{L_j} via

$$c_{L_j}^{(p+1)} = |c_{L_j}^{(p)} - \epsilon \sum_i K_{ij}^{(p)} (\Delta n_i - \Delta n_i^{\mathrm{DEMG}(p)})| \tag{18}$$

where $\Delta n_i^{\mathrm{DEMG}}(\{c_i, L_i\})$ is the predicted birefringence at t_i, ϵ is a small parameter, and p denotes the iteration number. K_{ij} and $\Delta n_i^{\mathrm{DEMG}}$ are calculated numerically by evaluating eqs 5, 6, 8, 11, 16, and 17 in each iteration. Thus, K_{ij} starts as an approximation and improves as $\{c_{L_i}\}$ improves. The adjustments continue until $\Delta n_i^{\mathrm{DEMG}}$ matches the measured Δn_i. In the language of inverse integral problems, this is a nonnegatively regularized solution of $\{c_{L_i}\}$.[46,47]

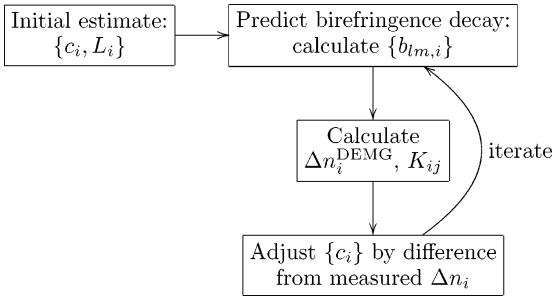

Figure 2. Schematic fitting method.

The method is shown schematically in Figure 2, and as shown below, it has been successful in fitting the measured birefringence decays.

3. Experimental Section

3.1. β-lg Fibril Preparation. All experiments were performed on bovine β-lg obtained from Sigma (L-0130-5G, batch 033K7003, a mixture of genetic variants A and B). The protein was dissolved in dilute hydrochloric acid at pH 2 and extensively dialyzed with the same pH 2 hydrochloric acid to remove traces of calcium ions and obtain a solution with the same ionic strength as the solvent (10 mM). The solution was centrifuged at 22600*g* for 30 min and filtered through a 0.45 μm filter to remove aggregates and undissolved protein. A UV spectrophotometer was used to measure the concentration of this stock solution, using a calibration curve from known β-lg concentrations, determined at a wavelength of 278 nm. The stock was used to make 10 mL samples under various conditions. The measurements presented are from a sample which was made at 5 mg/mL concentration and 0.01 M ionic strength. It was heated in a glass vessel for 24 h at 80 °C using a water bath, during which it was stirred constantly with a magnetic stirrer. A solution of fibrils was formed which was refrigerated at 4 °C for 24 h before measuring. Samples formed in this way were ideal for our measurements since they were transparent and without suspended spherulites (large aggregates of typical diameter 50 μm or greater[12,48]). They also gave large flow birefringence with slow decays and low noise, which were good for our analysis.

The concentration of unconverted protein was measured following the method of Aymard et al.[13] as adapted by Veerman et al.[45] An aliquot of the fibril solution was taken and the pH adjusted to the isoelectric point, pH 4.8. This causes the fibrils to aggregate, and these are removed by centrifugation at 22600*g* for 30 min. The β-lg concentration of the remaining solution is measured by UV spectrophotometry. Doubts over the accuracy of this method have emerged recently,[11] and the implications are discussed in section 4.4.

3.2. Rheooptical Technique. Birefringence experiments were performed on a strain-controlled ARES rheometer (Rheometrics Scientific) equipped with an optical analysis module. The system has undergone development by Klein et al.[49] to increase the sensitivity, reduce the background (residual birefringence in the optical train), and give better angle measurements. All measurements were performed in Couette geometry with a static inner bob of diameter 32 mm and rotating outer cup of diameter 33.8 mm. A laser beam of wavelength 670 nm passes between the cup and bob through 20 mm of sample. In this arrangement, the apparatus was capable of measuring birefringence Δn down to 10^{-8} at a sampling frequency of 24 times per second. The disadvantage of this geometry is that it requires 8 mL of sample—a large quantity in protein science.

The sample was subjected to steady shear at shear rates in the range 0.1−200 s^{-1}. Times between 30 s and 3 min at constant shear proved to be long enough to reach and measure a steady state for these shear rates. Decay in stopped flow was measured after shearing the sample steadily for 60 s. The decays were repeated several times so that they could be averaged to reduce the noise error. (Samples prepared in

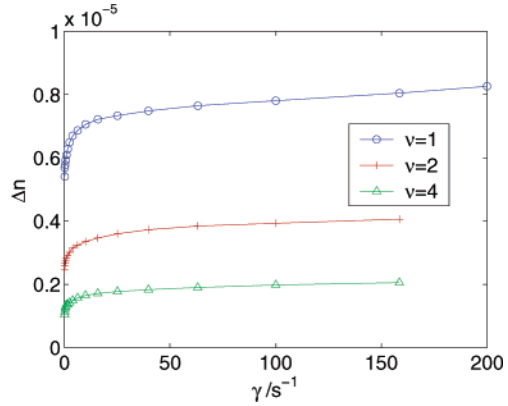

Figure 3. Steady shear birefringence Δn as a function of shear rate γ for different dilutions of the β-lg fibril solution. Data points are connected with straight lines for visualization.

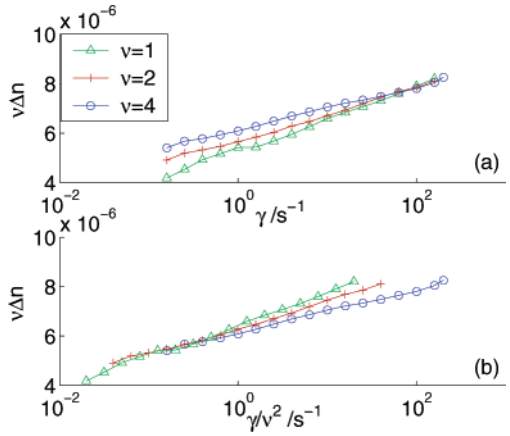

Figure 4. Steady shear birefringence for different dilutions of the β-lg fibril solution, scaled according to the dilute (a) and semidilute (b) regimes.

different conditions produced decay curves with various characteristic times from immeasurably short ($\ll$1 s) to several minutes and longer. The preparation described above was used to provide a sample with a sufficiently slow decay but one which is also liquid and optically clear.) The apparatus was kept at 20 °C in an air-conditioned room.

3.3. Imaging of Fibrils by TEM. The fibril solution was diluted to a concentration of 1 mg/mL and applied to a grid covered with a carbon-coated Formvar support film. The excess solution was removed by wicking with filter paper after 30 s. A droplet of 2% uranyl acetate solution was applied to negatively stain the fibrils, and the excess was removed after 15 s. Electron micrographs were taken using a Phillips CM 12 transmission electron microscope operating at 80 kV.

The TEM grid preparation was carried out within 24 h of the rheooptical measurements, during which period the sample was refrigerated at 4 °C.

4. Results and Analysis

4.1. Birefringence under Steady Shear. Figure 3 shows birefringence under steady shear for the solution. Measurements from the undiluted sample ($\nu = 1$) and the sample diluted to a half ($\nu = 2$) and a quarter ($\nu = 4$) of the original concentration (in pH 2 hydrochloric acid) are shown. At low shear rates, the birefringence increases sharply with γ and appears to be reaching a plateau where the fibrils are totally aligned. Figure 4 shows the steady shear birefringence on a log−linear plot, scaled according to both the dilute or concentration-independent regime (a) and the semidilute regime (b) (eqs 13 and 14). At low γ the curves meet when scaled

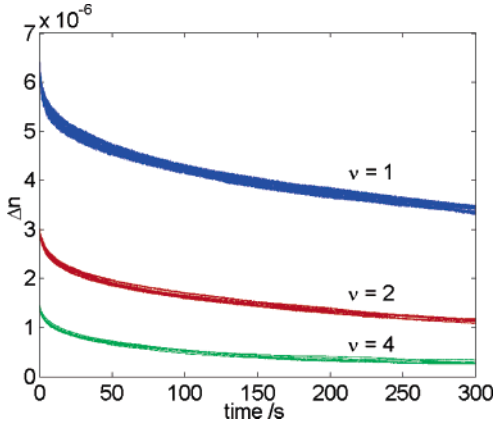

Figure 5. Successive birefringence decays from $\gamma = 5$ s^{-1} for different dilutions of the β-lg fibril solution. Six decays were measured at each dilution.

according to the semidilute regime but at high γ according to a dilute or concentration-independent regime. Therefore, neither regime describes the system perfectly, but rather the system appears to transit from semidilute to concentration-independent behavior as γ is increased.

This can be explained if all fibrils long enough to be in the semidilute regime tend toward complete alignment at increasing shear rates, so that for $\gamma > 20$ s^{-1} they contribute a negligible increase in $\Delta n(\gamma)$. The further increase in Δn with shear rate is then due only to processes which are independent of concentration. These are the alignment of fibrils which are shorter than the entanglement length L^* and therefore in the dilute regime, or the stretching of fibrils which are already aligned. Thus, dilute scaling is valid in this region. However, for $\gamma < 1$ s^{-1} the contribution of these processes is small, and the main dependence of $\Delta n(\gamma)$ is due to the increasing alignment with γ of fibrils sufficiently long to be in the semidilute regime.

These curves allow us to choose and justify a shear rate to use in the study of decays of section 4.2. A shear rate of 5 s^{-1} is between the two regions identified above. It is large enough so that fibrils above L^* are approaching complete alignment but small enough so that the alignment of short fibrils or stretching of aligned fibrils is not exacerbated. Thus, it is a compromise between completely aligning the fibrils and avoiding the contribution of processes which cannot be fitted by the DEMG theory.

4.2. Decay Curves and Concentration Scaling. Figure 5 shows decay curves in stopped flow from the same solution. Successive decays from the undiluted and diluted solution are shown ($\nu = 1, 2, 4$). The shear rate was 5 s^{-1} in all cases, and six decay curves were measured for each dilution. The curves show a very good reproducibility between successive decays, and the differences are probably due to inhomogeneities in the optical path (e.g., spherulites or dust) as well as noise and the random drift of the laser. (In fact, we found that successive relaxations from all shear rates up to 200 s^{-1} were reproducible, which indicates that fibrils are not broken up at these rates.)

The curves in Figure 5 are scaled according to eq 13 in Figure 6. They fall onto a master curve as predicted by the DEMG theory, within the variability between successive decays described above, and except for the region $t < 1$ s, where we may be seeing the combined effects of the finite time taken for the flow to stop, the

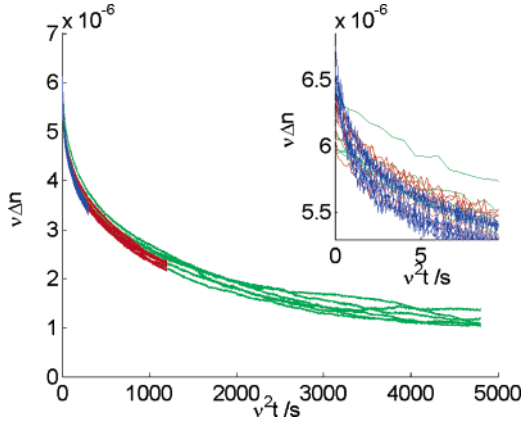

Figure 6. Decays for different dilutions of the β-lg fibril solution scaled according to the semidilute regime. Inset shows the detail of the first few seconds.

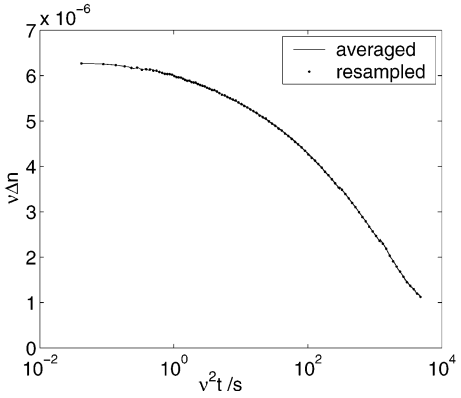

Figure 7. Averaged and resampled master decay curve of all data in Figure 6.

decay from the shorter end of the length distribution which is not in the semidilute regime and the relaxation of stretching modes of the fibrils (Figure 6 inset). There also seems to be a slight offset between the decay curves of each dilution which is not accounted for, but this is also within the variability between successive decays, so it is ignored.

The remarkable mutual closeness of the scaled curves confirms the assumptions that the fibrils diffuse like rods in the semidilute regime and that they are nonsticky and stable under dilution. We may now proceed to fit the master curve, although consideration must be made to errors from incomplete alignment, early times, and the short end of the distribution.

4.3. Length Distribution: Fitting the Decay Curves. The superposed curves of Figure 6 were averaged and resampled on a logarithmic time scale. The result is shown in Figure 7. The log−linear plot is instructive as it shows a maximum gradient at $t \sim 10^3$ s, so this is the dominant time scale of the decay, and a corresponding peak in the length distribution should be expected. Here we fit this curve according to the DEMG theory with 12 length components. At this stage, the constants β and M are still undetermined; therefore, the parameters $\{L'_i, c'_{L_i}\}$ instead of $\{L_i, c_{L_i}\}$ are taken, where

$$L'_i = (M^2\beta)^{-1/7} L_i \tag{19}$$

and

$$c'_{L_i} = M c_{L_i} \tag{20}$$

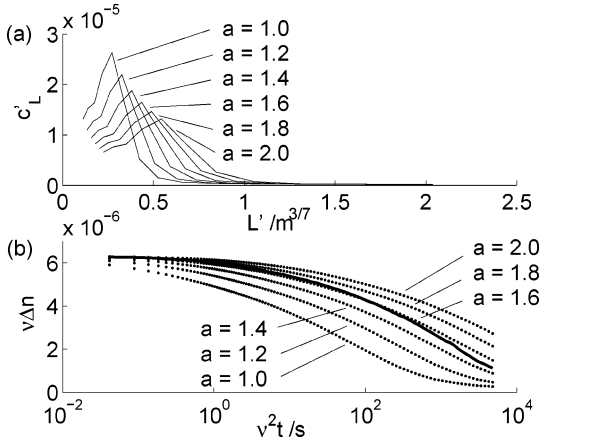

Figure 8. (a) Initial estimates of length distribution from inverse Laplace transformation, with lengths multiplied by various values of a. (b) Birefringence decay curves predicted by the same initial esimates. The master curve of Figure 7 is shown as a solid line.

This allows us to set $M = 1$ m^2 and $\beta = 1$ in our program. β and M will be evaluated by other methods in section 4.4 as a "calibration" to the length and concentration scales. Note that c'_{L_i} is dimensionless, and L'_i has the unusual dimensions of m$^{3/7}$ because it depends on M, though it is still only proportional to L_i.

A first estimate of $\{c'_{L_i}\}$ to fit the curve is found by taking an inverse Laplace transform: finding the $\{c'_{L_i}\}$ which satisfy

$$\Delta n_i = \sum_j e^{-s_i t_j} c'_{L_j} \tag{21}$$

where 12 points of the decay rates $\{s_i\}$ are sampled logarithmically between 1 s^{-1} and $1/(2t_{max})$, with $t_{max} =$ 4800 s. This procedure is described in detail in Appendix B. Now we choose $\{L_i\}$ to match $\{s_i\}$ according to the following approximation of eq 5:

$$L'_i = a\left(\frac{k_B T}{\eta(\sum_m c'_{L_m})^2 s_i}\right)^{1/7} \tag{22}$$

where a is an adjustable parameter of order 1. The resulting parameters$\{L'_i, c'_{L_i}\}$ are our initial estimate. A range of a between 1.0 and 2.0 gives the estimates shown in Figure 8a. These are each used to calculate a decay according to the DEMG theory (evaluating eqs 5, 6, 8, 11, 16, and 17) shown in Figure 8b. It must be noted that all distributions calculated in this paper are discrete. However, to achieve better visualization, we have plotted them as line graphs, where a unit of area under the graph is equivalent to a unit of length concentration, as it should be for a continuous distribution. This is detailed in Appendix C. The curve from $a = 1.6$ is closest to the measured curve, and thus it is the best starting point for fitting properly according to the DEMG theory. Following Chow and Fuller[34] our spherical harmonic coefficients $b_{lm,i}$ were truncated at $l = 12$. We found that this truncation makes negligible difference to the calculated decay curves.

In choosing our lengths in this way, the smallest length, L'_1 corresponds approximately to the decay time of 1 s, which is a good lower cutoff. It would not be meaningful to fit lower lengths than this since decays

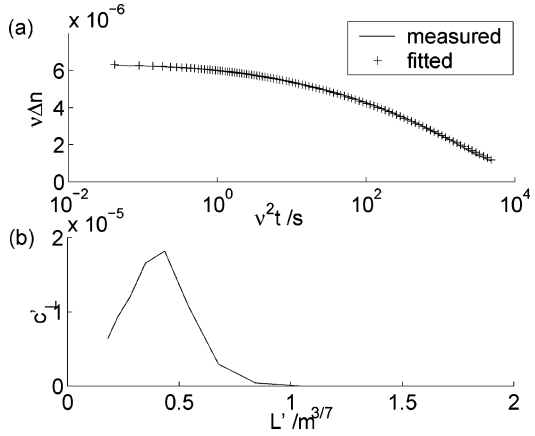

Figure 9. Master decay curve and fitted decay (a), with length distribution (b), after 1000 iterations from initial estimate with $a = 1.6$.

within this time are unaccounted for, as described above. We must also check that "calibrated" length L_1 is greater than the entanglement length L^*, which will be dealt with in section 4.4.

We proceed according to the method described in section 2.4, taking 1000 iterations with the small parameter

$$\epsilon = \frac{1}{20}\sqrt{\frac{\sum_i (\Delta n_i - \Delta n_i^{\mathrm{DEMG}})^2}{\sum_i \Delta n_i^{\,2}}} \qquad (23)$$

This produces the length distribution in Figure 9. As can be seen, the fit with measured data is good and adequately within the noise for the full length of the decay curve. The length distribution shows a clear peak which tails off in both directions. Therefore, our chosen range of $\{L'_i\}$ is adequately wide: any longer or shorter components included in the distribution will be fitted with small weight since there is no significant discrepancy between the measured and fitted decay at long or short times.

The fitting can be started from different initial estimates in order to test the stability of the fit within the measurement noise. We may fit from both directions (larger and smaller length) by using the estimates given by inverse Laplace transformation with $a = 1.4$ and $a = 1.8$. The results after 1000 iterations are shown in Figure 10. Another initial estimate is a delta funtion length distribution at $L' = 0.48$ m$^{3/7}$. This took 10000 iterations to converge and also leads to approximately the same distribution (Figure 10). This is encouraging for such an extreme initial estimate and shows that the ambiguity of fitting within the noise is modest. The fits agree with each other inasmuch as the same peak position and coarse shape of the distribution is reached.

A similar approach may be followed to assess the errors due to the finite limits and noncontinuity of the $\{L'_i\}$ range. We fit the curve with the following altered parameters, using the original initial estimate with $a = 1.6$: (i) $s_1 = 10$ s^{-1}, i.e., lower length cutoff chosen to correspond to a decay time of 0.1 s; (ii) $s_{12} = 1/(1.5t_{\max})$, i.e., upper length cutoff chosen to correspond to a decay time of $1.5t_{\max}$; (iii) 6 points in set $\{L'_i\}$, and (iv) 20 points in set $\{L'_i\}$. The results are plotted in Figure 11

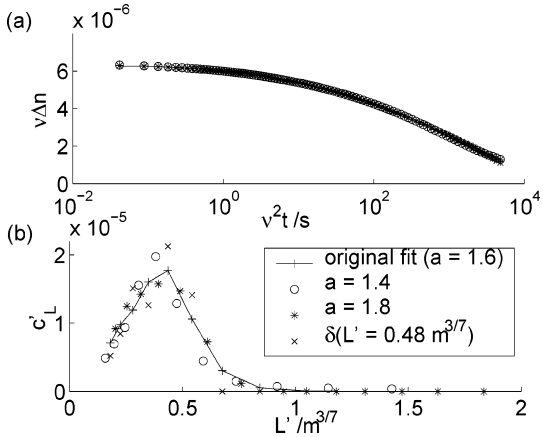

Figure 10. Master curve and fitted decays (a), with length distributions (b), starting from various initial estimates.

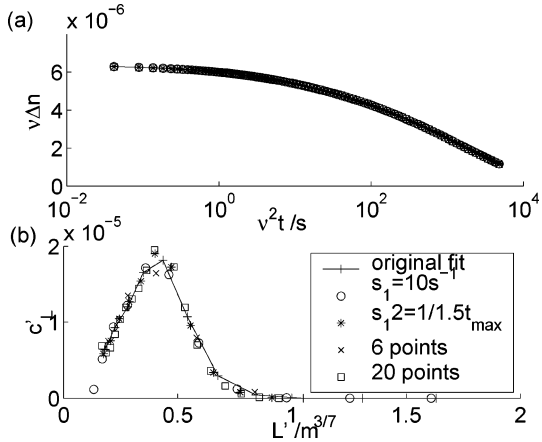

Figure 11. Master curve and fitted decays (a), from length distributions (b), on altered length arrays.

and show small variability compared to the fits from different initial estimates.

The variability of the fitted lines can be used as an estimate of the fitting error: we use the maximum devation above and below the original fitted line (of $a = 1.6$), at each point, to give the upper and lower fitting error (see section 4.5).

4.4. Comparison with TEM and Sedimentation Measurements: Calibrating the Length and Concentration Scales. M may be evaluated by calculating the total length concentration of fibrils. For this we use the fibril line density (number of proteins per unit length) of 0.28 nm^{-1}, as measured by SANS.[13] We measured the concentration of converted monomers in our sample following the method described in section 3.1. This consists of removing the fibrils and measuring the concentration of protein left in solution. From this, fibril concentration = 3.1 mg/mL for the conditions used. Thus, the total length concentration is 3.1×10^3g m^{-3} $\times N_A/(0.28\ \mathrm{nm}^{-1} \times 18.3\ \mathrm{kDa}) = 3.64 \times 10^{14}$ m^{-2}, where N_A is Avogadro's number. Using the assumption that all fibrils are perfectly aligned at $t = 0$, $\Delta n(0) = M\sum_i c_{L_i}$. Therefore, $M = 1.74 \times 10^{-20}$ m^2.

Unfortunately, the assay above is of questionable accuracy, mainly since the concentration of converted protein it yields may be larger than the actual fibril concentration. This is because it relies on aggregating and sedimenting the fibrils at the isoelectric point. An unknown amount of unconverted monomers as well as nonfibrillar aggregates may also be sedimented. Be-

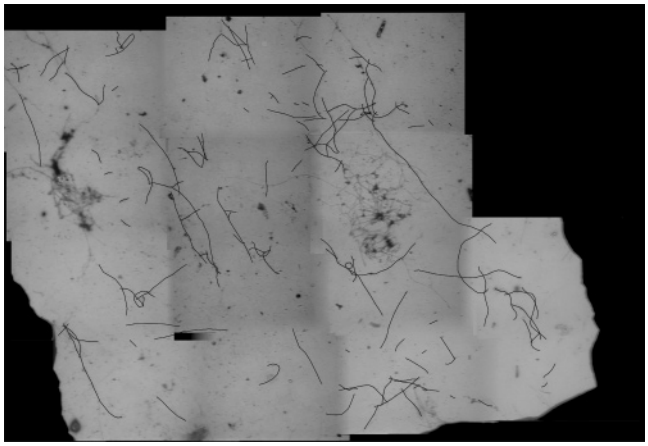

Figure 12. Composite TEM micrograph of β-lg fibrils from the solution. Measured fibrils are highlighted in black.

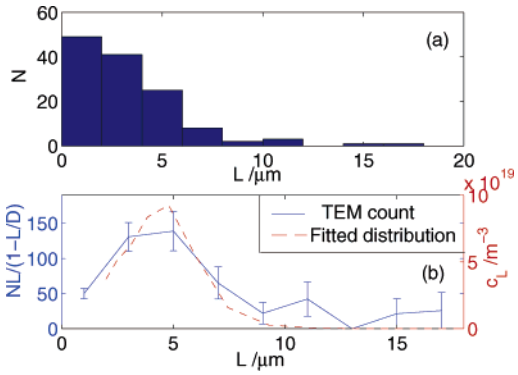

Figure 13. (a) Histogram of fibril lengths measured in the TEM composite (Figure 12). (b) Comparison of the length distributions from fitted birefringence decay and TEM allows "calibration" of the length scale.

cause of this, it would not be surprising if our value of M is significantly different from the real value. There will also be an error due to our assertion of $\Delta n(0) = M\sum_i c_{L_i}$, since there is also a contribution to $\Delta n(0)$ of the alignment of short fibrils (shorter than our chosen L_1) and stretching modes of longer fibrils. The line density may also be erroneous.[13]

However, we are not so interested in *absolute* concentration, and the method is still valid for *relative* concentrations, both in the sense of different samples and different lengths. In this work, the length scale will be calibrated by comparison of the length distribution with TEM measurements and adjustment of the factor $M^2\beta$; thus, it is not affected by the uncertainty in concentration (which is absorbed by β).

A composite image of fibrils from the sample was made by capturing 14 TEM micrographs and overlapping them (see Figure 12). The contour lengths of 130 fibrils were measured; this was the set of all fibrils which could be clearly distinguished and have both ends on the composite. (These are highlighted in black.) A histogram is made of the lengths, shown in Figure 13a. The statistical error on the count N is given by $\delta N = \sqrt{N}$ assuming random sampling. To compare this with the fitted distribution, N and δN must be weighted by length L to give a number proportional to length concentration. They must also be weighted by $1/(1 - L/D)$, where $D = 50$ μm, the width of the composite image. This is to correct for the dependence on L of the probability of both ends of a fibril of length L being found on the composite. The resulting histogram is plotted in Figure 13b and compared with the length distribution fitted from birefringence decay in the previous section (Figure 9).

A factor of $(M^2\beta)^{1/7} = 1.1 \times 10^{-5}$ m$^{4/7}$ has been chosen so that the peak of the histogram coincides with our fitted distribution. The correspondence between the distributions is good, with approximately the same shape given by both. The fitted distribution is slightly narrower than the TEM distribution, and besides the errors discussed in this article, it may reflect a scaling of diffusivity with length which is slightly less than that of the DEMG model. According to our measurement of M above, $\beta = 6.5 \times 10^4$, which is of the expected order of magnitude.[35,37]

Thus, our length and concentration scales are "calibrated", and this calibration is used for the distributions of the following sections.

It remains to check that the L^* is significantly less than our lower length cutoff. Using eq 7, our value of M gives $L^* = 52.4$ nm, which is much less than $L_1 = 2.0$ μm as required.

4.5. Estimation of Errors. Assuming the master decay curve is governed exactly by the DEMG theory, the length distribution arrived at in the previous section accounts for it well, within limitations to accuracy set by the calibration of length and concentration by other methods, the noise of measurement, and resulting ambiguity of fitting. However, these are not all the sources of error, and we have already commented on the assumptions and approximations that led to this stage. To summarize, they are (1) sample motion stops instantaneously at $t = 0$, (2) perfect alignment of fibrils of length $\geq L_1$ at $t = 0$, and (3) no contribution due to unaccounted-for decay processes: alignment of fibrils shorter than L^* or stretching modes.

Of course, the sample does not stop instantaneously according to 1 but requires a finite time. The flow decays with a characteristic time $\tau = d^2\rho/\eta$, where $d = 0.9$ mm the gap width of the cell, $\rho \approx 10^3$ kg m^{-3} the density of water, and $\eta \sim 10^{-2}$ Pa s for the undiluted sample at $\gamma = 5$ s^{-1} according to the rheometer. Thus, $\tau \sim 0.1$ s, which we will take as instantaneous for time scales greater than a second. We can also estimate the stop time by examining the stress relaxation according to the rheometer. The stress decays to within the noise level in about 1 s (data not shown).

The effect of this finite stop time on the scaled decay curve will be to slow down decays within approximately the first second for the undiluted sample and the first 4 s and 16 s for the diluted samples, which partially explains why the semidilute scaling does not perfectly describe the decays in this region. We can estimate the resulting error due to this finite stop time by fitting a master decay curve which has been altered so that, in the first second, the birefringence decays instantaneously, followed by a linear extrapolation of the decay at $t = 1$ s. The result is shown in Figure 14.

Approximations 2 and 3 were made possible by the choice of $\gamma = 5$ s^{-1} as a compromise between completely aligning the fibrils and avoiding unaccounted-for decay processes. Figure 4 shows that above $\gamma = 20$ s^{-1} the steady shear birefringence converges onto a master curve according to the dilute regime, showing that fibrils of $L > L^*$ are completely aligned. Therefore, we may estimate the error due to incomplete alignment of the fibrils of $L \geq L_1$ by fitting a decay curve which starts from $\Delta n(\gamma = 20\ \text{s}^{-1}) \approx 7.1 \times 10^{-6}$ and follows our

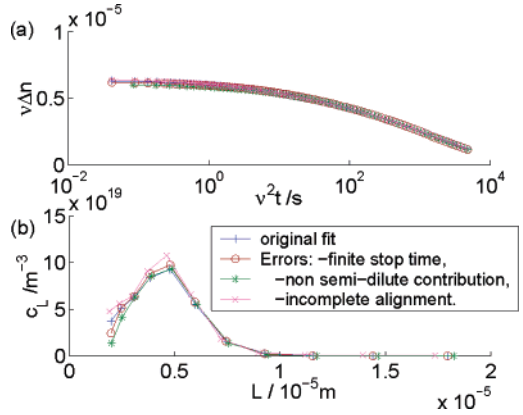

Figure 14. Errors in the fitted length distribution caused by errors in our assumptions. Maximum changes to the measured data from the effects of finite stop time, a non semidilute contribution to the decay, and incomplete alignment at $t = 0$ were estimated (a) and fitted (b).

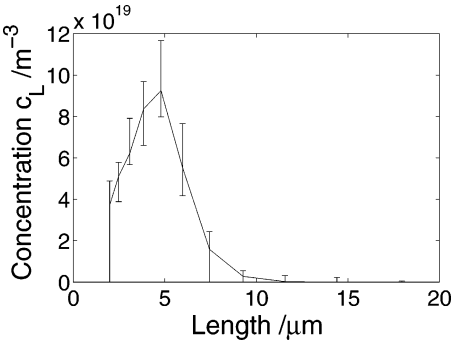

Figure 15. Length distribution of β-lg fibrils in solution, as fitted from birefringence decay, with total errors due to ambiguity of fitting and estimated errors in assumptions.

measured curve at $t > 0$, thus approximating the maximum additional contribution (see Figure 14).

Figure 4 also shows that below $\gamma = 1\ s^{-1}$ the steady shear birefringence converges onto a master curve according to the semidilute regime, showing that there is minimal contribution of the alignment of fibrils of $L < L^*$ and stretching modes. Therefore, we may estimate the error due to these unaccounted-for effects by fitting our master decay curve, but starting from a time t where $\Delta n(t) = \Delta n(\gamma/\nu^2 = 1\ s^{-1}) \approx 6.0 \times 10^{-6}$. Thus, we make an estimated correction of the maximum contribution of this effect (see Figure 14).

All three of these estimates only affect the low end of the length distribution significantly, which is to be expected because they are based on assumptions which affect early times.

The upper and lower total error from these sources and the fitting error are estimated by taking the square root of the sum of squares of positive and negative deviations from the original fit. These are plotted as vertical error bars in Figure 15.

Figure 15 shows the result of our technique. We have extracted, from birefringence relaxation data, a length distribution of an amyloid fibril system, which compares well with the length distribution obtained by microscopy. The estimated errors are small enough so that the shape of the distribution is unambiguous on a coarse level. For our sample, the length distribution is singly peaked at 5 μm with a full width at half-maximum of 4 $\pm$ 1 μm. It is not possible to say whether there is a maximum length in the distribution; this is chiefly due to the truncation of the decay at 4800 s, which results in an ambiguity of fitting the longer lengths. Information is also absent on lengths $\leq 2\ \mu$m due to experimental limitations. However, the position and width of the peak in the distribution are valuable measurements which this technique can offer.

5. Conclusion

We have developed a promising technique for measuring the length distribution of a rodlike system, which can potentially be applied to any fibril system whose orientational relaxation can be resolved in time. In the results presented, the decay was measured across 4 decades of time, allowing length concentration to be measured across almost a decade of length. This was enough to capture the peak in the length distribution of our fibril system. The high power dependence of rotational diffusivity on length in the semidilute regime leads to the disadvantage that it has been necessary to measure such a wide range of time in order to get a modest distribution of length. It also leads to the advantage that the relaxation at each time is dominated by a corresponding length; thus, the error due to ambiguity in fitting the curve is modest, as we have shown.

In an idealized system of rods whose lengths tend to infinity and diameter tends to zero, it can be seen that the semidilute regime is valid for all concentrations. In our system and many other interesting ones, the rodlike objects are of small and well-defined diameter, but large and arbitrary length. Therefore, we argue that our method, based on the dynamics of the semidilute regime, may be applicable to many other systems. As a relaxation method, it is distinguished from dynamic light scattering in that it is applicable to systems which do not scatter light significantly, which is the case for these thin rods of volume $\ll$ (wavelength)^3. It could also be applied to dichroic systems by measuring flow dichroism, instead of birefringence, which would make no difference to the analysis.

Another experimental possibility is alignment by an electric field, from which very short decay times could be resolved without the problem caused by the finite time taken for the flow to stop. In this way, the technique could potentially be applied to much shorter rods.

In the particular case of the β-lg amyloid system we have studied, the length distribution should be able to yield clues as to the kinetics of fibril assembly. This subject is under further investigation.

Acknowledgment. We thank Harry Baptist for his patient assistance with TEM imaging and the Virology Department of Wageningen University for use of their TEM facilities. We also gratefully acknowledge funding from the BBSRC for S.S.R. and the European Commission for an IHP grant awarded to the Food Physics Group of Wageningen University for a Marie Curie Training Site Fellowship (Contract HPMT-2000-00188). S.S.R. also thanks Pietro Cicuta for a very fruitful suggestion, Sir Sam F. Edwards for illuminating discussions, and Mark Blomsma for hospitality in Wageningen during some of the experiments.

Appendix A. Coordinate Frame and Spherical Harmonics

The orientational distribution $\psi(\mathbf{u})$ can be expanded in spherical harmonics in the usual spherical polar

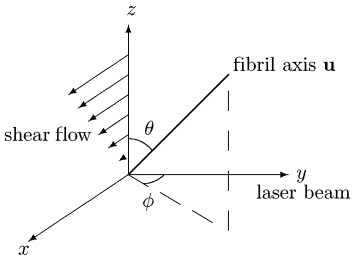

Figure 16. Defined coordinates, showing direction of shear flow and direction of propagation of light.

coordinates (Figure 16): $\psi(\mathbf{u}) = \sum_{lm} a_{lm} Y_l^m(\theta,\phi)$. Light is defined as propagating along the y axis, and shear flow takes place in the xz plane. Because of this flow, $\psi(\mathbf{u})$ will have reflection symmetry in the xz plane; therefore

$$a_{lm} = (-1)^m a_{l-m} \tag{24}$$

so our set of spherical harmonics can be replaced with

$$|l,m) = \begin{cases} Y_l^0 & \text{for } m = 0 \\ \dfrac{Y_l^m + Y_l^{-m}}{\sqrt{2}} & \text{otherwise} \end{cases} \tag{25}$$

such that

$$\psi(\mathbf{u}) = \sum_{lm} b_{lm} |l,m) \tag{26}$$

and the coefficients b_{lm} are used instead of a_{lm}.

For a shear flow of velocity $\gamma z\hat{x}$ in this coordinate frame, Γ, the differential operator yielding the differential change in $\psi(\mathbf{u})$ per unit time, per unit γ, is

$$\Gamma = \cos^2\theta \cos\phi \frac{\partial}{\partial\theta} - \cot\theta \sin\phi \frac{\partial}{\partial\phi} - 3 \sin\theta \cos\theta \cos\phi \tag{27}$$

The matrix elements $(l, m|\Gamma|l', m')$ of eq 8 are calculated in ref 31.

Appendix B. Inverse Laplace Transform Estimate of the Length Distribution

The initial estimate of $\{c'_{L_i}\}$ is made by inverting eq 21 with the following method, following Chapter 18.5 in ref 46. First, a solution is made by zeroth-order linear regularization, solving the following equation by LU decomposition:

$$\sum_j (\sum_i e^{-(s_k+s_j)t_i} + \lambda\delta_{kj}) c'_{L_j} = \sum_i e^{-s_k t_i} \Delta n_i \tag{28}$$

which is a set of N equations in N unknowns, where

$$\lambda = \frac{1}{N} \sum_{ij} e^{-2s_j t_i} \tag{29}$$

Second, we apply the regularizing condition that $c'_{L_i} \geq 0$ by using the iterative equation

$$c'^{(p+1)}_{L_k} = |c'^{(p)}_{L_k} - \epsilon \sum_j (\sum_i e^{-(s_k+s_j)t_i} + \lambda\delta_{kj}) c'^{(p)}_{L_j} + \epsilon \sum_i e^{-s_k t_i} \Delta n_i| \tag{30}$$

where we take the small adjustment parameter

$$\epsilon = 2/\text{max eigenvalue}(\sum_i e^{-(s_k+s_j)t_i} + \lambda\delta_{kj}) \tag{31}$$

1000 iterations were enough to closely fit the curve.

Appendix C. Plotting a Discrete Distribution in a Continuous Form

All fitted distributions of $\{L_i, c_{L_i}\}$ are discrete. However, the real length distribution is continuous, and the results are far better visualized in a continuous form. To do this, a set of midpoints of length $\{L_i^{\text{mid}}\}$ are plotted against the weighted interpolated length concentrations$\{c_{L_i}^{\text{mid}}\}$, where

$$L_i^{\text{mid}} = \frac{1}{2}(L_{i+1} - L_i) \tag{32}$$

and

$$c_{Li}^{\text{mid}} = \frac{\frac{1}{2}(c_{L_i+1} + c_{L_i})}{L_{i+1} - L_i} \tag{33}$$

The graphs produced are true distributions in the sense that unit area under the line is equivalent to unit c_L, and this transformation is exact as $L_{i+1} - L_i \to 0$.

References and Notes

(1) Lashuel, H. A.; LaBrenz, S. R.; Woo, L.; Serpell, L. C.; Kelly, J. W. *J. Am. Chem. Soc.* **2000**, *122*, 5262.
(2) Sunde, M.; Serpell, L.; Bartlam, M.; Fraser, P.; Pepys, M.; Blake, C. *J. Mol. Biol.* **1997**, *31*, 729.
(3) Dobson, C. M. *Trends Biochem. Sci.* **1999**, *24*, 329.
(4) Kelly, J. *Curr. Opin. Struct. Biol.* **1998**, *8*, 101.
(5) Dobson, C. *Philos. Trans. R. Soc. London B* **2001**, *356*, 133.
(6) Hardy, J.; Higgins, G. *Science* **1992**, *256*, 184.
(7) Bucciantini, M.; Giannoni, E.; Chiti, F.; Baroni, F.; Formigli, L.; Zurdo, J.; Taffei, N.; Ramponi, G.; Dobson, C.; Stefani, M. *Nature (London)* **2002**, *416*, 507.
(8) Rochet, J.; Lansbury, P., Jr. *Curr. Opin. Struct. Biol.* **2000**, *10*, 60.
(9) Gosal, W. S.; Clark, A. H.; Pudney, P. D. A.; Ross-Murphy, S. B. *Langmuir* **2002**, *18*, 7174.
(10) Bromley, E. H. C.; Krebs, M. R. H.; Donald, A. M. *Faraday Discuss.* **2005**, *128*.
(11) Arnaudov, L.; de Vries, R.; Ippel, H.; van Mierlo, C. *Biomacromolecules* **2003**, *4*, 1614.
(12) Sagis, L. M. C.; Veerman, C.; van der Linden, E. *Langmuir* **2004**, *20*, 924.
(13) Aymard, P.; Nicolai, T.; Durrand, D. *Macromolecules* **1999**, *32*, 2542.
(14) Nazhad, M.; Ramos, L.; Paszner, L.; Saddler, J. *Enzyme Microb. Technol.* **1995**, *17*, 68.
(15) Molin, U.; Lennholm, H. *Appita J.* **2001**, *54*, 540.
(16) Furtado, C.; Kim, U.; Gutierrez, H.; Pan, L.; Dickey, E. C.; Eklund, P. C. *J. Am. Chem. Soc.* **2004**, *126*, 6095.
(17) Islam, M.; Rojas, E.; Bergey, D.; Johnson, A.; Yodh, A. *Nano Lett.* **2003**, *3*, 269.
(18) Balasubramanian, C.; Godbole, V.; Rohatgi, V.; Das, A.; Bhoraskar, S. *Nanotechnology* **2004**, *15*, 370.
(19) Lin, J.; Chou, C.; Lin, J. *Macromol. Rapid Commun.* **2004**, *25*, 1109.
(20) Kosmulski, M.; Durand-Vidal, S.; Maczka, E.; Rosenholm, J. *J. Colloid Interface Sci.* **2004**, *271*, 261.
(21) Baron, P. *Ind. Health* **2001**, *39*, 39.
(22) Grosse, I.; Huetter, B.; Hartmann, I.; Binde, G.; Gruber, H.; Kurz, G. *J. Hazardous Mater.* **1998**, *63*, 119.
(23) Donaldson, K.; Tran, C. *Mutat. Res.* **2004**, *553*, 5.
(24) Brown, W., Ed. *Dynamic Light Scattering: The Method and Some Applications;* Oxford University Press: New York, 1993.
(25) Vermant, J.; Yang, H.; Fuller, G. *AIChE J.* **2001**, *47*, 790.
(26) Wierenga, A.; Philipse, A.; Reitsma, E. *Langmuir* **1997**, *13*, 6947.

(27) Kramer, H.; Deggelmann, M.; Graf, C.; Hagenbtichle, M.; Johner, C.; Weber, R. *Macromolecules* **1992**, *25*, 4325.
(28) Morris, V.; Foweraker, A.; Jennings, B. *Adv. Mol. Relax. Interact. Processes* **1978**, *12*, 211.
(29) van der Linden, E.; Sagis, L.; Venema, P. *Curr. Opin. Colloid Interface Sci.* **2003**, *8*, 349.
(30) Fuller, G. *Optical Rheometry of Complex Fluids;* Oxford University Press: New York, 1995.
(31) Doi, M.; Edwards, S. F. *J. Chem. Soc.*, *Faraday Trans. 2* **1978**, *74*, 918.
(32) Marrucci, G.; Grizzuti, N. *J. Polym. Sci.*, *Polym. Lett. Ed.* **1983**, *21*, 83.
(33) Marrucci, G.; Grizzuti, N. *J. Non-Newtonian Fluid Mech.* **1984**, *14*, 13.
(34) Chow, A. W.; Fuller, G. G. *Macromolecules* **1985**, *18*, 786.
(35) Pecora, R.; Tracy, M. A. *Annu. Rev. Phys. Chem.* **1992**, *43*, 525.
(36) Maeda, T. *Macromolecules* **1990**, *14*, 1464.
(37) Odell, J.; Keller, A.; Atkins, E. *Macromolecules* **1985**, *18*, 1443.
(38) Jain, S.; Cohen, C. *Macromolecules* **1981**, *14*, 759.
(39) Chow, A. W.; Fuller, G. G. *Macromolecules* **1985**, *18*, 793.
(40) Sun, Y.; Luo, Z.; A.; F.; K. N.; A. *Biochem. Biophys. Res. Co.* **2002**, *295*, 382.
(41) Hofmann, H.; Voss, T.; Kuhn, K.; Engel, J. *J. Mol. Biol.* **1984**, *172*, 325.
(42) Nestler, F.; Hvidt, S.; Ferry, J. *Biopolymers* **1983**, *22*, 1747.
(43) Sagis, L. M. C.; Veerman, C.; Ganzevles, R.; Ramaekers, M.; Bolder, S. G.; van der Linden, E. *Food Hydrocolloids* **2002**, *16*, 207.
(44) MacRaild, C. A.; Hatters, D. M.; Lawrence, L. J.; Howlett, G. J. *Biophys. J.* **2003**, *84*, 2562.
(45) Veerman, C.; Ruis, H.; Sagis, L. M. C.; van der Linden, E. *Biomacromolecules* **2002**, *3*, 869.
(46) Press, W.; Flannery, B.; Teukolsky, S.; Vetterling, W. *Numerical Recipes in C*, 2nd ed.; Cambridge University Press: New York, 1993.
(47) Provencher, S. *Makromol. Chem.* **1979**, *180*, 201.
(48) Krebs, M.; MacPhee, C.; Miller, A.; Dunlop, I.; Dobson, C.; Donald, A. *Proc. Natl. Acad. Sci. U.S.A.* **2004**, *101*, 14420.
(49) Klein, C.; Donald, A. M.; van Dusschoten, D.; van der Linden, E.; Rogers, S. S.; Sagis, L.; Venema, P.; Wilhelm, M., manuscript in preparation.

MA0474224